High Temperature Oxidation Behavior of ODS Ferritic Stainless Steel Fe-16Cr-4Al-1Ni-0.4Y_2O_3

Hakimul Wafda[1,2*], Djoko Hadi Prajitno[3], Eddy Agus Basuki[4], Ahmad Syafiq[4],
Nina Widiawati[1], and Asril Pramutadi Andi Mustari[2]

[1]Center for Nuclear Reactor Technology, National Research and Innovation Agency (BRIN),
KST BJ Habibie, Serpong, Tangerang Selatan 15310, Indonesia

[2]Nuclear Science and Engineering Study Program, Institut Teknologi Bandung, Jl. Ganesa No. 10, Bandung 40132, Indonesia

[3]Center for Radiation Process Technology, National Research and Innovation Agency (BRIN),
KST BJ Habibie, Serpong, Tangerang Selatan 15310, Indonesia

[4]Metallurgical Engineering Study Program, Institut Teknologi Bandung, Jl. Ganesa No. 10, Bandung 40132, Indonesia

*** Corresponding author:***

tel: +62-87770008830
email: haki003@brin.go.id

Received: April 2, 2024
Accepted: May 17, 2024

DOI: 10.22146/ijc.95284

Abstract: *This study investigates the isothermic oxidation behavior of the new ODS alloy Fe-16Cr-4Al-1Ni-0.4Y_2O_3 (% by weight) at 700, 800 and 900 °C, with exposure times of 5, 20, 50, and 100 h at each temperature. The purpose is to obtain new data on its high-temperature parabolic oxidation constant for assessing oxidation resistance. The methods used include isothermal oxidation testing, XRD, SEM-EDS characterization, and analysis of oxidation kinetics by monitoring changes in oxide thickness using microscopy and SEM-EDS. The oxide products formed on the sample surface are Fe_2O_3, Fe_3O_4, $AlFe_2O_4$, and $(Fe,Cr)_2O_3$. Al and Cr oxides are located under the dominant Fe oxide layer on the surface of the sample. The oxidation test results showed that the most protective sample was obtained at a temperature of 700 °C for 100 h with an oxide thickness of 263.99 μm. The kinetics analysis correlates strongly with the parabolic equation ($R^2 \approx 1$). The oxidation rate constants at temperatures of 700, 800, and 900 °C were 681.76, 2957.5, and 12300 $\mu m^2\ h^{-1}$, respectively. The activation energy required by the oxidation reaction in this alloy is 136.5 kJ mol^{-1}. This research enhances understanding and potential applications of the Fe-16Cr-4Al-1Ni-0.4Y_2O_3 alloy in high-temperature environments.*

Keywords: *ODS; oxidation resistance; high temperature; oxide thickness*

■ INTRODUCTION

The future demand for energy is substantial, necessitating the advancement of power plants that are both environmentally friendly and highly efficient. Among these is the fission reactor generator, which has now entered Generation IV [1-2]. Ongoing research and development efforts dedicated to Generation IV reactors are focused on overcoming challenges related to safety, environmental impact, and material properties, all within an academic context [3]. Progress in cladding material development is fundamental to the high efficiency and extended burnup operation of Generation IV. The primary objective of utilizing these materials as cladding is to confine the fuel and fission products within the fuel pin, ensuring the secure and reliable operation of the reactor [4-6]. Cladding materials must withstand elevated temperatures, corrosive conditions, and exposure to neutron environments typical of advanced nuclear systems [7-8]. This resilience is crucial for the long-term viability and effectiveness of Generation IV reactors.

Several materials, including oxide dispersion strengthened (ODS) steels—especially those with a high chromium content—have been recognized as promising options for fuel cladding in advanced nuclear systems [9-11]. ODS ferritic steels, distinguished by elevated chromium levels, have shown potential for deployment in environments marked by high temperatures, corrosion, and neutron exposure conditions commonly encountered in Generation IV nuclear energy systems [10-12].

The austenitic Fe-Cr-Ni-Al alloys exhibit higher toughness and resistance to plastic deformation due to the formation of an adherent oxide layer. The presence of oxide dispersion in Fe alloys improves oxidation resistance by enhancing the adhesiveness of the oxide layer. Studies show that doping with elements such as Ti, Zr, V, or Y results in a smooth and well-bonded oxide layer. Rare earth elements and other reactive elements play a crucial role in enhancing oxidation resistance by facilitating better adhesion between the oxide layer and the substrate, as well as reducing the rate of oxide growth [13-14].

This paper is dedicated to a comprehensive investigation into the high-temperature oxidation behavior of the new ODS ferritic stainless steel Fe-16Cr-4Al-1Ni-0.4Y_2O_3, with a specific emphasis on its suitability as a cladding material for next-generation nuclear reactors. The successful integration of ODS alloys in nuclear reactor designs promises enhanced safety margins, prolonged component lifetimes, and increased operating temperatures, all of which are crucial for the advancement of nuclear energy technology [11,15].

However, malfunctioning of generating equipment can lead to overheating, resulting in the actual temperature being higher than the operating temperature [16]. The targeted operating temperature and pressure are 625 °C and 25 MPa, which are expected to increase annually [17]. The elevated temperature makes the materials used susceptible to oxidation, potentially causing the failure of the generating vessel. Therefore, a material capable of withstanding these conditions is crucial [18-20].

ODS materials were developed because they meet criteria such as ductility, crack toughness, resistance to neutron radiation, and resistance to extreme corrosion at high temperatures [21-25]. ODS utilizes stable oxides that are very fine and evenly dispersed in the matrix. Oxide particles do not react with the alloy, thereby restraining grain growth or the dislocation pinning effect and reducing grain coarsening during exposure to high temperatures [26-27].

Research on ODS of the ferritic type with the composition Fe-16Cr-4Al-1Ni-0.4Y_2O_3 has previously been carried out with a series of in-depth studies ranging from the manufacturing process to microstructural studies. The recommended variables for milling, powder-ball ratio, compacting, and sintering are as follows: 120 min for milling, a powder-ball ratio of 1:10, compacting at 100 kgf cm^{-2}, and sintering at 1000 °C, respectively [28-29]. This research will continue with isothermic oxidation testing of alloys that have been made optimally with temperature variations of 700, 800, and 900 °C and several variations of exposure time. This research enhances understanding and potential applications of the Fe-16Cr-4Al-1Ni-0.4Y_2O_3 alloy in high-temperature environments. This study aims to investigate the isothermal oxidation behavior of ferritic ODS steel containing Y_2O_3 dispersoids at elevated temperatures, aiming to provide valuable insights for developing ODS ferritic steels. The findings from this research are expected to have implications for the potential application of these materials in high-temperature environments, particularly in future nuclear reactors.

■ EXPERIMENTAL SECTION

Materials

All chemicals for the alloy synthesis were commercially available with a purity of at least 99%: Fe powder Merck, 150 µm, 99%), Cr powder (Sigma Aldrich, 45 µm, 99%), Al powder (Merck, Art. 1056, 99%), Ni powder (Merck, 10 µm), and Y_2O_3 powder measuring 70 nm.

Instrumentation

The alloying and mixing processes were conducted using a planetary ball mill with stainless steel ball grinding media of 8 and 12 mm in size. The compaction process utilized a compaction machine at a pressure of 40 kN (499 MPa), producing samples with a diameter of 10 mm and a thickness of 8 mm. Subsequently, the sintering process was performed in a furnace at a temperature of 1000 °C for 6 h under inert conditions. Isothermal oxidation was carried out using a horizontal tube furnace. X-ray diffraction (XRD) analysis was conducted with a Rigaku SmartLAB XRD machine and scanning electron microscopy with energy dispersive spectroscopy (SEM-EDS) was performed using a Hitachi SU3500-AMATEX APOLLO XL. Hardness testing was executed with a load of 100 gf using a Vickers Hardness Test Machine in accordance with ASTM E384 standards.

Procedure

The metal alloy was prepared according to the composition (% by weight) 78.6Fe-16Cr-4Al-1Ni-0.4Y_2O_3 with a total weight of 26 g. Mechanical alloying (MA) was carried out using a planetary ball mill at a speed of 1290 rpm for 2 h and employing 8 mm and 12 mm SS steel ball grinding media. The resulting powder blend was compacted at a pressure of 40 kN for 4 min into a sample measuring 10 mm in diameter and 3 mm thick. Subsequently, the samples were sintered at 1000 °C for 6 h under inert conditions using a horizontal tube furnace. Isothermic oxidation was conducted using a horizontal tube furnace with temperature variations of 700, 800, and 900 °C. Tests were performed with variations in exposure time to oxidation for 5, 20, 50, and 100 h for each temperature variation. Initial samples, before undergoing oxidation testing, were characterized using optical microscopy (OM) and SEM-EDS, to assess the formed phases, percentage porosity, and sample homogeneity. Hardness was determined by conducting microindentation tests with a 100 gf load using the Vickers Hardness Test Machine (ASTM E384). Following oxidation, the samples underwent analysis for the formed oxide products using XRD. Subsequently, the surface morphology and cross-section of the samples were examined using SEM-EDS equipped with X-ray mapping features. Furthermore, the thickness of the oxide scale on each sample was measured using OM.

■ RESULTS AND DISCUSSION

Preliminary Analysis of ODS Alloys

The alloy, resulting from mechanical alloying for 120 min and sintered for 6 h at 1000 °C, exhibits a flat grain morphology and is relatively smaller in size than the initial state, owing to the fracturing process during milling, as illustrated in Fig. 1. However, some grains undergo cold welding during milling, causing them to be larger than their initial size. The presence of this cold welding pattern indicates that there is diffusion between the powders during the milling process, utilizing plastic deformation that results in atomic vacancies. These vacancies facilitate easier atom diffusion, revealing that the integration process can occur through milling without requiring the smelting process.

In previous studies, at a compaction pressure of 0.1 kN, the achieved porosity was reported as 11.024% [28]. With an increase in pressure to 40 kN in our study, the porosity of the ODS alloy sample decreased to 5.865%. This aligns with the theory that higher compaction pressure results in lower density. Furthermore, it can be inferred that this as-sintered alloy has reached the final stage of the sintering process since its porosity has reduced to less than 8%.

On the other hand, the decrease in porosity also increases the hardness value of the alloy matrix, which is 321.13 HV from the previous 119 HV [28]. Porosity can act as a stress concentration and is very effective as a starting point for cracks. So, with reduced porosity, the alloy can become stronger when external stress is received. The hardness is directly proportional to the yield stress of the alloy. Therefore, increasing the value of this hardness can increase the strength of the alloy, as shown in previous studies.

The as-sintered sample exhibits a composition relatively consistent with the original composition, and

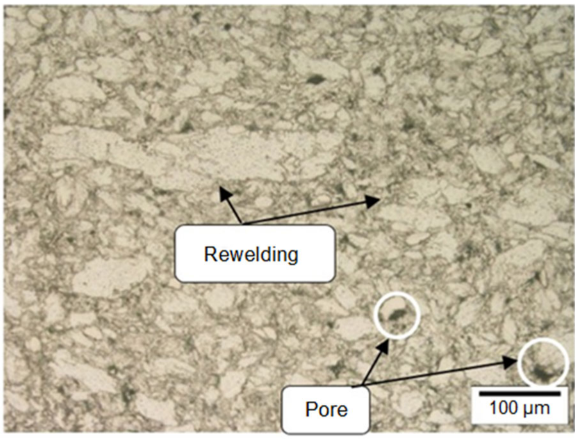

Fig 1. Results of OM and SEM observations of as sintered ODS alloys

it is evenly distributed, with the exception of a small number of clumpy Cr grains resulting from suboptimal mechanical blending. According to the EDS results, the element percentages were 5.79% Al, 0.41% Y, 12.55% Cr, 71.98% Fe, and 0.77% Ni. Notably, there are oxygen inclusions accounting for 8.5%, concentrated at the grain boundaries, as observed in the X-ray mapping shown in Fig. 2. These diffused oxygen atoms can become trapped in the alloy during compaction or mechanical alloying. Consequently, during sintering, O_2 gas ionizes into O^{2-} ions and dissolves at the grain boundaries.

Isothermic Oxidation Behavior at 700 °C

In the 700 °C isothermic oxidation test, the dominant Fe oxide is formed on the surface of the ODS alloy, as depicted in the XRD diffractogram in Fig. 3. The identified Fe oxide products include hematite (Fe_2O_3) and magnetite (Fe_3O_4). In the 5-h sample, an additional oxide, spinel hersinite ($AlFe_2O_4$), was detected. However, this oxide disappeared over time, as evidenced in the diffractogram of the 100-h sample. The XRD results in Fig. 3 reveal a relatively similar pattern in the diffractograms at the 5th and 100th h. The prevalence of Fe oxide in both samples can be attributed to the abundant availability of Fe in the matrix, which is also the main element constituting the ferritic matrix. Kinetically, the diffusion of Fe^{2+} or Fe^{3+} ions is more dominant than other alloying elements. Fe^{2+} ions react with O^{2-} ions to initially form FeO, aligning with literature indicating that FeO forms at temperatures above 570 °C. However, XRD did not detect FeO. The porous nature of FeO allows it to undergo reactions with other oxides, forming spinel and solid solutions, topics to be discussed in the next sub-chapter. Additionally, FeO is oxidized to Fe_3O_4, which forms a coat on the surface above it and oxidizes back to Fe_2O_3, coating the outermost surface. This process occurs rapidly, and by the 5th h, the Fe_2O_3 compound was observed to dominate the surface, becoming more pronounced with extended

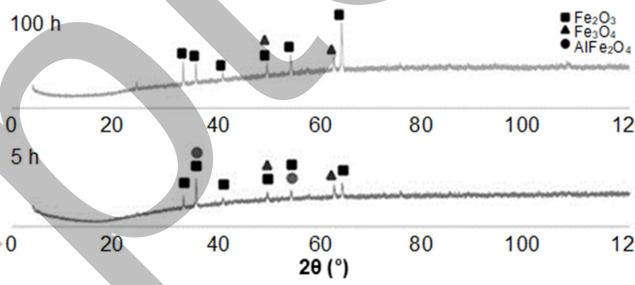

Fig 3. The diffractogram of XRD analysis results of oxidation samples at temperatures of 700 °C

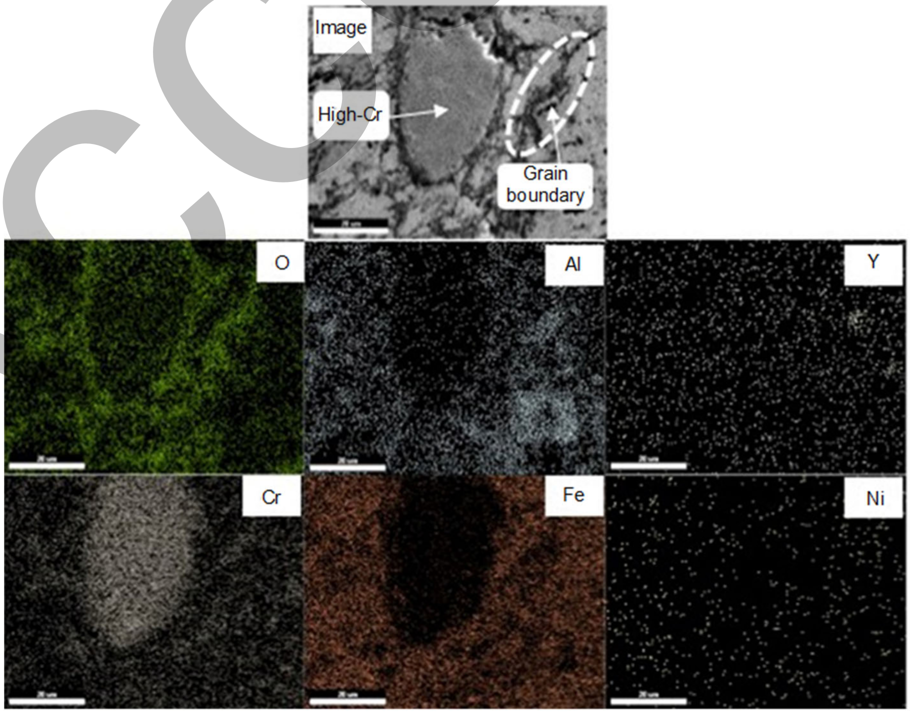

Fig 2. The distribution of alloying elements in the as sintered sample using the X-ray mapping method

oxidation time. Ni and Cr are not visible in the XRD results because a phase change occurs when heated at high temperatures. This causes Ni and Cr to likely dissolve into Fe, forming the A-phase (Fe,Cr), which will not be visible in the XRD data. Additionally, Ni also dissolves into Fe.

Fe oxides are generally non-stoichiometric, allowing easy oxygen diffusion and rapid formation of oxides with other alloying elements. In this alloy, Cr and Al have the potential to form their respective oxides. However, only $AlFe_2O_4$ was detectable by XRD, observed at the 5th h, whereas Cr oxide couldn't be detected due to its relatively low concentration. This is evident in the X-ray mapping results, where the density of Cr atoms is relatively less than that of Al atoms.

From a thermodynamic perspective, aluminum is the most easily oxidized element, as indicated by the oxide equilibrium diagram in the Ellingham diagram. Furthermore, in the 50-h sample mapping as shown in Fig. 4, Cr and Al atoms are observed beneath the Fe oxide crust. This positioning hinders $Cu\text{-}K_\alpha$ XRD radiation from reaching these atoms. The limitation of XRD is also reflected in Fig. 3 for the 100th h sample, where the $AlFe_2O_4$ spinel could not be detected. In essence, the absence of an optimal layer protecting the alloy allows the continued diffusion of Fe^{2+}, resulting in the thickening of the oxide layer on the surface. The suboptimal protection of the $AlFe_2O_4$ layer is attributed to the limited availability of Al in the substrate.

The morphology of the oxide layer on the surface of the alloy was observed using SEM at the beginning and end of the test, as illustrated in Fig. 5. In the 5-h sample, oxide crystals grew in needle-shaped and blade-shaped structures, identified as Fe_2O_3 compounds. Initially, the oxide grew rapidly and heterogeneously, resulting in the growth of only a portion of the dominant crystals. As time progressed, in the 100th h sample, the oxide growth became more homogeneous, presenting a denser and smoother appearance.

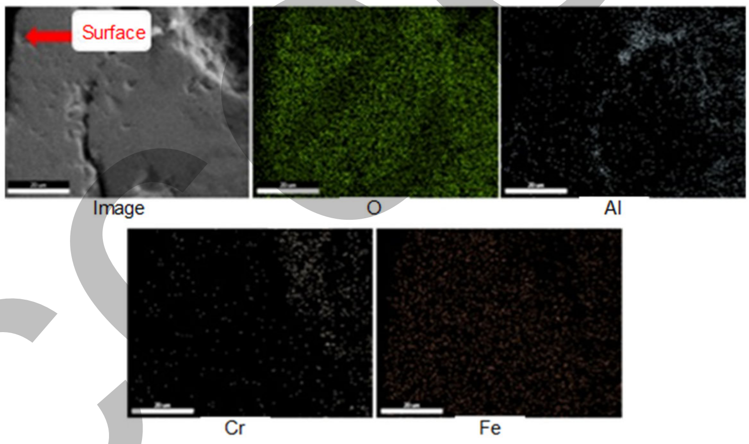

Fig 4. X-ray mapping analysis of cross-sectional samples of oxidation test results at 700 °C for 50 h

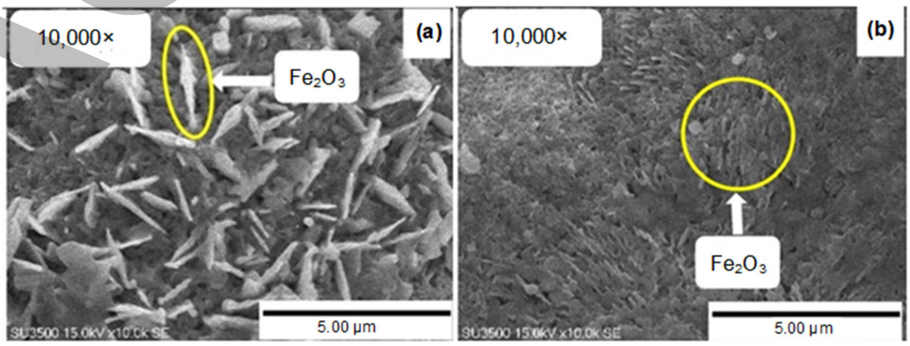

Fig 5. Surface morphology of the oxide at 700 °C for (a) 5 h and (b) 100 h

Isothermic Oxidation Behavior at 800 °C

At a temperature of 800 °C, the oxidation products observed from the diffractogram, as presented in Fig. 6, are relatively similar to the oxidation products at 700 °C, namely hematite, magnetite, and hersinite. However, at the 100th h, hersinite was not found and only two peaks indicating Fe_2O_3 and Fe_3O_4 were observed. The morphology of hersinite was successfully observed at this temperature using SEM on a slightly spalled oxide surface, as shown in Fig. 7. Hersinite formed in the colonies, creating islands just below the layers of Fe_2O_3 and Fe_3O_4. This oxide plays a crucial role in inhibiting the diffusion of Fe ions from the metal to the outer oxide-oxygen interface in the air, minimizing the thickening of Fe oxide.

In the study of Fe-5%Al alloy between 700 and 900 °C, hersinite was not found in the oxide scale, and the Al oxide product tended to be in the form of α-Al_2O_3 [30]. However, the depleted Al content in this alloy causes the formed Al_2O_3 to become unstable and react with the higher concentration of Fe_3O_4 oxide, as shown in Eq. (1) and (2). Other research has also detailed that during oxidation at 800 °C in the Fe-2%Al alloy, there is loss of the Fe_3O_4 layer. At 800 °C, Al oxide begins to form, initiating a chemical reaction between the alumina layer and Fe_3O_4, leading to the production of spinel $FeAl_2O_4$ [31]. In our study, a relatively higher number of Fe_3O_4 layers were formed, allowing their detection in XRD analysis. Moreover, the presence of less alumina results in a different spinel, namely $AlFe_2O_4$, as explained by the reaction below. Eq. (1) also explains the reason for the loss of FeO, as it reacts with alumina to form spinel. Both of these reactions continue until enough $AlFe_2O_4$ is formed, effectively protecting against the diffusion of Fe ions.

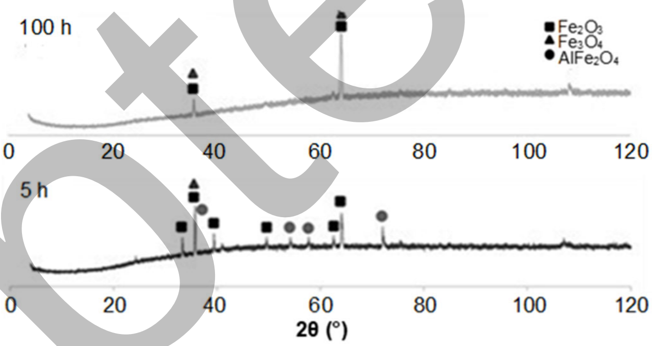

Fig 6. The diffractogram of XRD analysis results of oxidation samples at temperatures of 800 °C

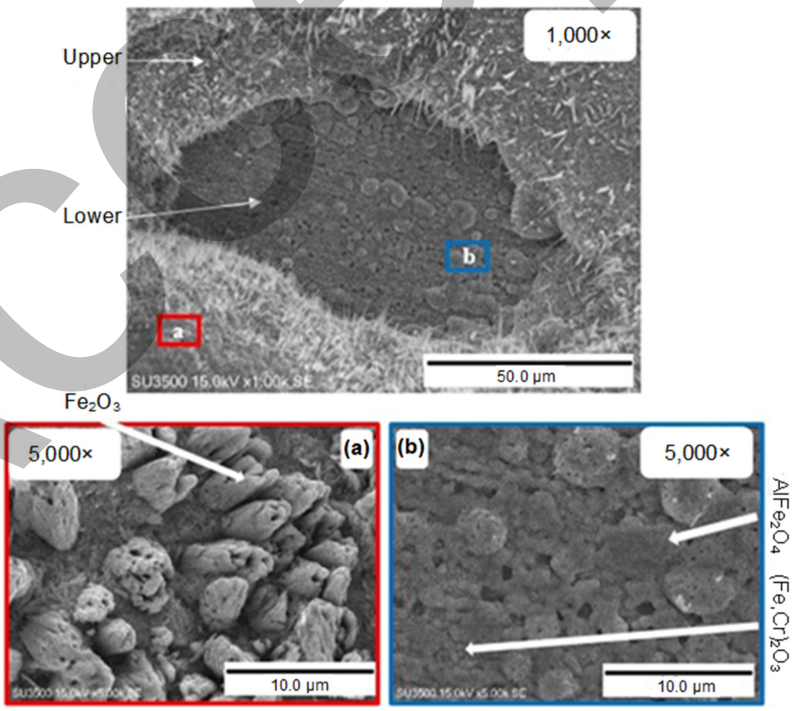

Fig 7. Observation on slightly spalled alloy parts of surface morphology of (a) top layer (Fe oxide) and (b) bottom layer containing Al and Cr oxide at 800 °C for 5 h

$$7FeO + Al_2O_3 + O_2 \rightarrow 2AlFe_2O_4 + Fe_3O_4 \quad (1)$$

$$2Fe_3O_4 + Al_2O_3 \rightarrow 2AlFe_2O_4 + Fe_2O_3 \quad (2)$$

The Cr content in the substrate was also identified through SEM, and mapping results depicted the bottom layer's morphology. As illustrated in Fig. 8, the mapping results indicate that the compact layer has a relatively dominant Fe and Cr content. This dominance can be attributed to the composition of the initial alloy, which constitutes a matrix of α-(Fe,Cr) or solid solution. Notably, Basuki [28] demonstrated that during the 1.5 h MA process, a ferritic solid solution (α-Fe) was formed, with no Cr peak detected. These findings suggest that with an extended MA time, the blending process occurs more optimally, increasing the dissolved Cr content.

In another literature, it is noted that the oxide α-Cr_2O_3 shares isostructural compounds with α-Fe_2O_3 and several others. These shared structural properties enable the formation of solid solutions through the mechanism of cation substitution in the two isomorphic compounds, involving Fe(III) and Cr(III) ions [32]. Consequently, the oxidation reaction to form a solid solution $(Fe,Cr)_2O_3$ can be expressed as Eq. (3);

$$2\alpha - (Fe,Cr) + \frac{3}{2}O_2 \rightarrow (Fe,Cr)_2O_3 \quad (3)$$

Cr and Al oxides at 800 °C are easier to observe than at 700 °C. This is due to the higher temperature, the more diffusion of Cr and Al ions, so it can become a protective layer to inhibit further oxidation over time. In the SEM observations of the alloy at the 100th h, as depicted in Fig. 9, the surface texture of the oxide appears more uniform compared to the start of the test, shown in Fig. 7(a), with the same SEM magnification of 5,000 times. Initially, the crystalline form of Fe oxide does not seem needle-shaped but rather porous and forms random columns, as illustrated in Fig. 7(a). These variations in the growth patterns of Fe oxide crystals are reasonable and influenced by factors such as alloying composition and impurities in the constituent matrix. In his book, Cornell explains that hematite can take various shapes, including plates, pseudocubes, nuts, needles, and spindles. Even under ideal conditions, hematite has a hexagonal triplet Fe–O–Fe structure [32].

The difference in impurities in the matrix is caused by oxidation behavior at 800 °C, indicating that O^{2-} ions can diffuse more into the alloy than at 700 °C. Another factor influencing growth is the environment. In this case, the temperature of 800 °C does not appear to affect crystal growth significantly, allowing for a more even surface coverage over an extended period.

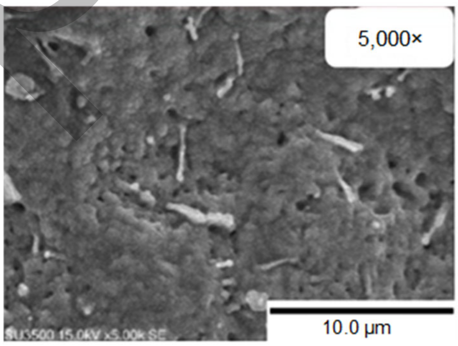

Fig 9. Surface morphology at 800 °C for 100 h

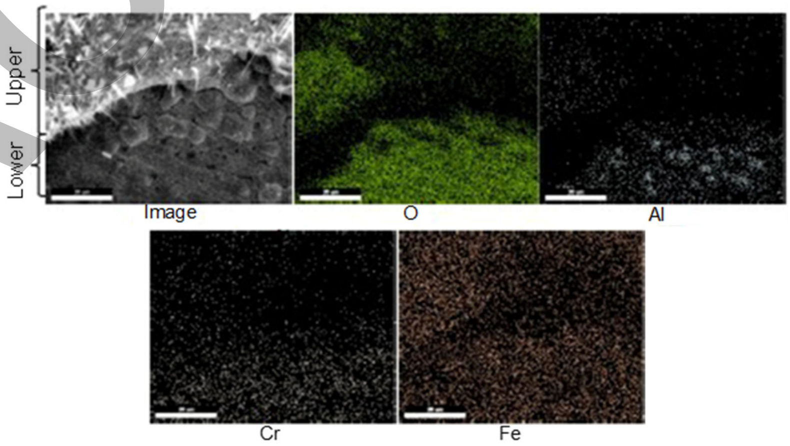

Fig 8. X-ray mapping analysis of the morphology of the samples from the oxidation test at 800 °C for 5 h

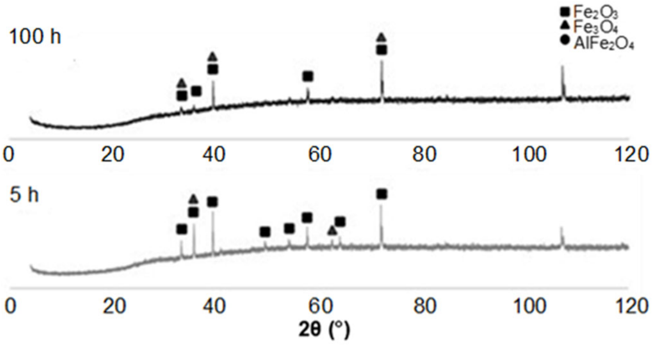

Fig 10. The diffractogram of XRD analysis results of oxidation samples at temperatures of 900 °C

Isothermic Oxidation Behavior at 900 °C

At a temperature of 900 °C, the resulting oxide product differs significantly from the previous temperature. The absence of hersinite spinel from the initial test is shown in Fig. 10. Only two oxides were detected throughout the test duration: Fe_2O_3 and Fe_3O_4. The absence of Al oxide was detected due to the thickness of the oxide layer that was formed. Notably, at the 5th h, the oxide thickness was higher compared to the thickness at the 100th h at 700 °C. This observation indicates that, up to a thickness of 290 μm, the $AlFe_2O_4$ protective layer is not present in very small amounts. The lack of a protective layer on the surface results in continuous oxidation of the alloy. Al and Cr oxides were, in fact, detected beneath the surface of the Fe oxide layer, as shown in Fig. 11. The reason for the absence of Al and Cr layers near the surface is attributed to the colonies formed not being able to protect them optimally. At a temperature of 900 °C, thermal stress can interfere with the growth of Al and Cr oxides, preventing them from forming tightly.

The absence of the Al and Cr oxide layers results in internal oxidation, as depicted in the layer above the alloy substrate in Fig. 12. This occurs due to Al and Cr depletion, reducing their content in the alloy substrate. Despite the initial presence of 4% Al, which should ideally lead to continuous Al_2O_3 oxide formation, Tomaszewicz [31] noted in his research that reducing Al levels below 2.2% could trigger internal oxidation, forming only an Fe oxide layer. The continuous formation of the Al_2O_3 layer is expected when the Al content exceeds 2.2%, with optimal effectiveness observed at levels exceeding 7.1%.

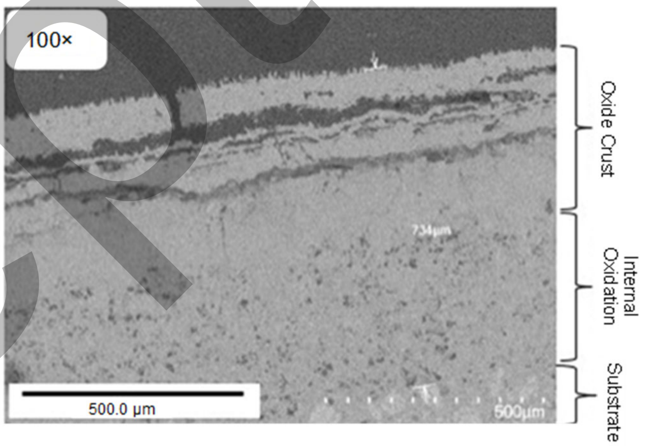

Fig 12. SEM cross-section of the alloy at oxidation temperature of 900 °C for 50 h

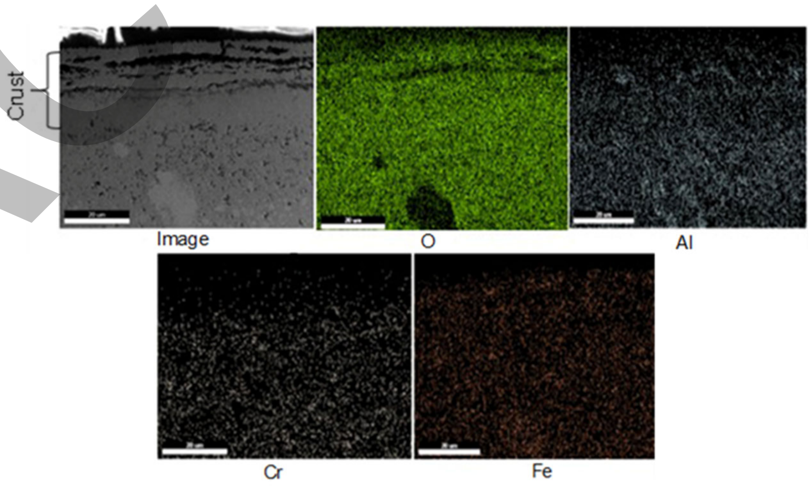

Fig 11. X-ray mapping cross-sectional cross-section of the sample from the oxidation test at a temperature of 900 °C, 50 h with a magnification of 60×, and a crust thickness of 755 μm

In addition to Al and Cr depletion, other factors contributing to this deep oxidation include grain boundaries and porosity. Thick grain boundaries containing Al_2O_3 and Cr_2O_3 can serve as pathways for O^{2-} ions to diffuse into the substrate. At a temperature of 900 °C, the diffusion movement is accelerated, facilitated by the increased temperature, which results in faster atomic movement, creating space or vacancies for ions to diffuse easily. Simultaneously, the presence of porosity during oxidation provides voids that aid in the diffusion of O^{2-} ions. The availability of space within the alloy significantly influences ion movement. Furthermore, in conjunction with defects in the substrate caused by the movement of Fe^{2+} ions, the alloy's porosity of 5.865% amplifies the dominance of O^{2-} ions in the diffusion balance.

SEM observations reveal a slightly different oxide structure compared to 800 °C, as shown in Fig. 7(b). In the 5-h sample observation, the crystal columns of Fe oxide tend not to form colonies and appear solid, with growth still appearing random, as depicted in Fig. 13(a). However, during the 100-h sample observation, the formed oxides did not overlap each other, as illustrated in Fig. 13(b). The higher temperatures contribute to more vacancies in the crust, inhibiting the growth of oxide crystals. As seen in Fig. 12, elongated cavities occur in the crustal area due to the buckling effect.

This buckling effect can occur when the volume of oxide formed is greater than the amount of metal consumed. In addition, the weak interfacial force between the crust and the substrate and the defects caused by oxygen inclusions during oxidation makes the scale easy to detach. The existence of this defect causes the growth of oxides on the surface not to take place evenly and not to form a tight layer. The crystal columns appear to be transformed into smaller diameters and are relatively rounded at the ends of the columns. This structural change can occur due to longer exposure times and higher temperatures, so crystals tend to form structures that have the smallest surface tension, such as balls.

Oxidation Kinetics of ODS 78.6Fe-16Cr-4Al-1Ni-0.4Y_2O_3 Alloy at High Temperature

A graph of oxide thickness against time is obtained from the three temperature tests, as shown in Fig. 14. With increasing test temperatures, the formed oxide becomes thicker. Visually, the pattern observed at temperatures of 700 and 800 °C indicates that, at the beginning of the test, oxidation was rapid, and as time progressed, the growth rate of the oxide decreased. In contrast, at 900 °C, there is no visible pattern of decreasing oxidation rate, and the rate is expected to decrease over an extended period due to the substantial thickness of the oxide.

The pattern evident in Fig. 14 corresponds to the parabolic kinetics graph, signifying that the oxidation process is governed by ion diffusion across the oxide crust [30]. Notably, as the oxide crust thickens, the rate of

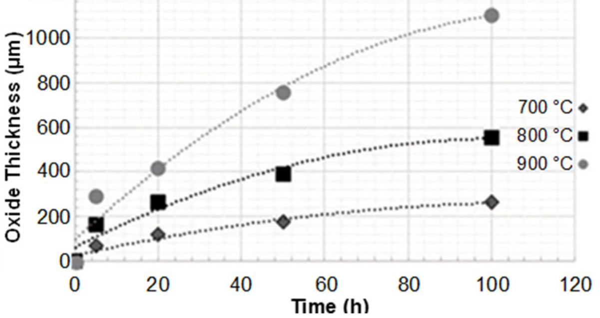

Fig 14. Profile thickness of the oxide

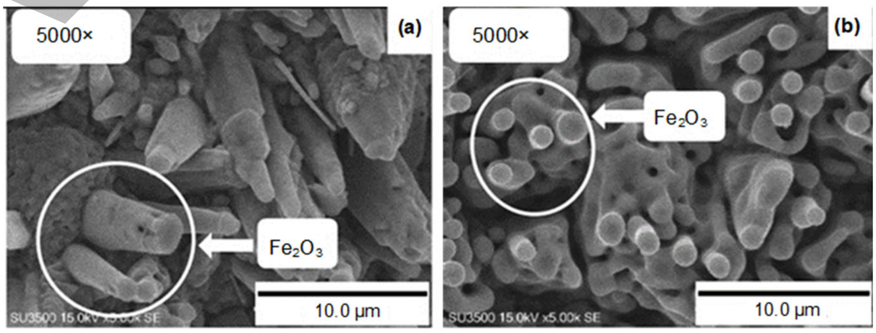

Fig 13. Oxide surface morphology at 900 °C for (a) 5 h and (b) 100 h

Table 1. Several types of oxidation rate equations and their constants

Temperature (°C)	Oxidation rate	Equation	Constant ($\mu m^2\ h^{-1}$)	R^2
700	Linear	$x = 1.9823t + 69.551$	1.9823	0.9897
	Parabolic	$x^2 = 681.76t - 174.38$	681.76	0.9922
	Logarithmic	$x = 61.612\ln t - 45.846$	61.612	0.9122
800	Linear	$x = 3.9973t + 168.39$	3.9973	0.9817
	Parabolic	$x^2 = 2957.5t + 9888.4$	2957.5	0.9994
	Logarithmic	$x = 126.07\ln t - 70.322$	126.07	0.9317
900	Linear	$x = 8.6629t + 263.94$	8.6629	0.9885
	Parabolic	$x^2 = 12300t - 24741$	12300	0.9939
	Logarithmic	$x = 265.66\ln t - 228.59$	265.66	0.8870

oxidation diminishes, indicating the prolonged diffusion time required for metal ions and oxides as the distance increases. The available data is fitted to the relevant kinetic rate equations to validate the proposed kinetic rate equation hypothesis. Utilizing the MS Excel interpolation program, we derive equations for each kinetic rate constant and R^2, as detailed in Table 1. The table underscores that the parabolic equation's R^2 is closer to 1 compared to the others, supporting its suitability for describing the observed oxidation kinetics.

The value of the oxidation rate constant for the parabolic equation in Table 1 is a specific value at certain temperatures. In general, that temperature-dependent value can be described by the Arrhenius equation as follows:

$$k = k_0 \exp\left(-\frac{Q}{RT}\right) \quad (4)$$

$$\ln k = \ln k_0 - \frac{Q}{RT} \quad (5)$$

where Q is the activation energy, and k_0 is a constant. Eq. (5) is a derivative of Eq. (4), which can be plotted linearly. The ensuing linear plot illustrates the relationship among the three parabolic rate constants of the ODS Fe-16Cr-4Al-1Ni-0.4Y_2O_3 alloy. From the slope of the graph, we can ascertain that the activation energy value is 136.5 kJ mol^{-1}.

The value of Q differs from one alloy to another. In other alloys, it is known that the Q values of T91-type steel and Al0,1CoCrFeNi high-entropy alloy (HEA) are 189 and 280 kJ mol^{-1}, respectively. The difference in the Q value indicates that the higher the activation energy, the greater the energy required, or, in other words, the oxidation reaction is more difficult to occur [33]. The ODS alloy in this study has the smallest value, and a larger oxide thickness supports this compared to other alloys. The thickness of the oxide in the HEA alloy and T91 steel is 4.80 and 100 μm, respectively. While the alloy in this study had a thickness above 100 μm at the end of the test at each temperature.

Oxide Growth Mechanism

Fig. 15 shows a theoretical schematic illustration of the isothermal oxidation mechanism of the ODS alloy in

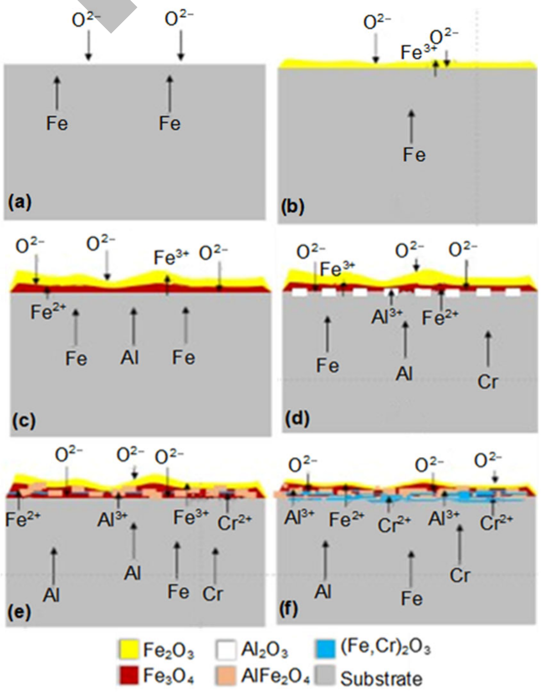

Fig 15. Illustration of the Oxide Growth Mechanism in the order (a), (b), (c), (d), (e), and (f) along with the length of time of exposure to oxidation

this study. The alloy's first oxidation process upon exposure to O^{2-} is depicted in Fig. 15(a). As oxygen atoms interact with the metal surface, a thin oxide layer is created. As discussed in the previous sub-chapter, Fe oxide will initially grow in the form of the Fe_2O_3 compound, coating the surface of the alloy, as depicted in Fig. 15(b). Upon the saturation condition occurring, O^{2-} ions are not able to oxidize optimally, leading to the formation of a layer of Fe_3O_4 right beneath the Fe_2O_3 layer, as shown in Fig. 15(c).

The FeO compound is actually formed but immediately reacts or is oxidized again. Under certain conditions, Al_2O_3 begins to grow in colonies at the Fe-metal interface spots and inhibits the interaction of oxygen with Fe, as shown in Fig. 15(d). However, the presence of relatively small amounts of Al_2O_3 will immediately disappear due to spontaneous reactions with FeO and Fe_3O_4 to form $AlFe_2O_4$ spinel, as seen in Fig. 15(e). The subsequent alloying element to undergo oxidation is Cr. However, Cr in the alloy substrate is a solid solution with Fe. Consequently, upon oxidation, the oxide formed takes the shape of a solid solution, namely $(Fe,Cr)_2O_3$. This oxide envelops the $AlFe_2O_4$ colony in the form of a thin layer, as illustrated in Fig. 15(e). Over an extended period, it is anticipated that the oxidation of Cr and Al elements will intensify, eventually forming a protective layer on the surface, as shown in Fig. 15(f). Simultaneously, the diffusion of Fe will be impeded, halting the oxidation process of the alloy.

Fig. 15 elucidates the mechanism of atomic diffusion from each metal atom on the alloy substrate. This atomic diffusion progresses through the existing vacancies until it reaches the metal-oxide interface. At this interface, ionization occurs, transforming the metal into its respective ion. The diffusion mechanism within the oxide transitions into an ion diffusion mechanism or defect diffusion. Metal cation ions diffuse through the existing defects and react with O^{2-} ions, which also undergo ion diffusion into the oxide. In Fig. 15(f), ion diffusion has commenced reaching equilibrium as the protective layers of $AlFe_2O_4$ and $(Fe,Cr)_2O_3$ become sufficiently thick. The sequence of the formed oxide layers is illustrated in Fig. 16. Spinel $AlFe_2O_4$ appears to be the first to form, followed by the solid solution oxide $(Fe,Cr)_2O_3$. This phenomenon can be attributed not only to the higher reactivity of Al towards oxygen but also to the fact that the atomic diffusion constant of solid oxide solutions (Fe and Cr) is considerably lower compared to the diffusivity of Al. Therefore, if the cross-section is cut, the order of the oxides from outermost to deepest is Fe_2O_3, Fe_3O_4, $AlFe_2O_4$, and $(Fe,Cr)_2O_3$.

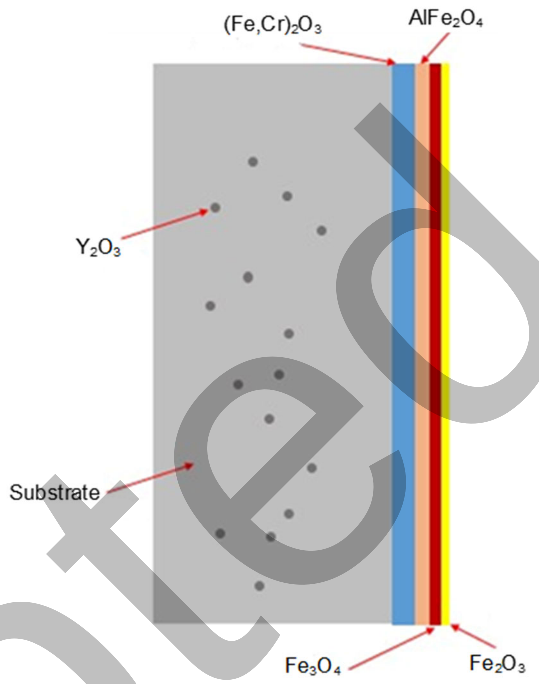

Fig 16. The arrangement of the oxide layer formed on the surface of the alloy

CONCLUSION

The ODS alloy in its sintered state demonstrates enhanced properties, characterized by a porosity of 5.865% and a hardness of 321.13 HV due to higher compaction pressure, which ranges from 0.1 to 40 kN. The rate of oxidation and oxide layer thickness increase with rising temperatures. The sample exposed to 700 °C for 100 h showed the best protection with a 263.99 µm thick layer. The sequence of oxide layers formed includes Fe_2O_3, Fe_3O_4, $AlFe_2O_4$, and $(Fe,Cr)_2O_3$. The oxidation rate of the ODS alloy follows the parabolic rate equation. The oxide layer thickness is crucial in controlling oxidation, with rate constants at 700, 800, and 900 °C measured at 681.76, 2,957.5, and

12,300.0 µm^2 h^{-1}, respectively. The activation energy for the reaction is 136.5 kJ mol^{-1}. Additionally, an extended duration of oxidation exposure leads to a decrease in the oxidation rate. This reduction can be attributed to the increased thickness and density of the oxide layer, which act as inhibiting factors for atom diffusion. In conclusion, the alloy composition with 16% Cr and 4% Al demonstrates effective protection against oxidation. The results are expected to offer valuable insights for the development of ODS ferritic steels by exploring the isothermal oxidation behavior of ferritic ODS steel containing Y_2O_3 dispersoids at elevated temperatures. These findings have implications for its potential application in high-temperature environments, such as future nuclear reactors.

■ ACKNOWLEDGMENTS

The authors would like to acknowledge the support from Center for Radiation Process Technology and Center for Nuclear Reactor Technology, National Research and Innovation Agency, as well as Metallurgical Engineering Study Program and Nuclear Science and Engineering Study Program, Institut Teknologi Bandung.

■ CONFLICT OF INTEREST

The authors declare no conflict of interest.

■ AUTHOR CONTRIBUTIONS

Djoko Hadi Prajitno: conceptualization, methodology, validation, writing-reviewing, and editing. Hakimul Wafda: conceptualization, methodology, validation, writing-reviewing, and editing. Eddy Agus Basuki: conceptualization, methodology, validation, writing-reviewing, and editing. Ahmad Syafiq: methodology, validation, writing-reviewing, and editing. Nina Widiawati: writing-reviewing and editing. Asril Pramutadi Andi Mustari: writing-reviewing and editing. All authors agreed to the final version of this manuscript.

■ REFERENCES

[1] Şahin, S., and Şahin, H.M., 2021, Generation-IV reactors and nuclear hydrogen production, *Int. J. Hydrogen Energy*, 46 (57), 28936–28948.

[2] Kelly, J.E., 2014, Generation IV International Forum: A decade of progress through international cooperation, *Prog. Nucl. Energy*, 77, 240–246.

[3] Stoica, L.N., Radu, V., Nitu, A.I., Prisecaru, I., 2021, Study of the Structural Mechanical Behaviour in Liquid Lead Environment for the ALFRED Generation IV Reactor, *10th International Conference on Energy and Environment (CIEM)*, Bucharest, Romania, 14-15 October 2021.

[4] Basuki, E.A., Adrianto, N., Triastomo, R., Korda, A.A., Achmad, T.L., Muhammad, F., and Prajitno, D.H., 2022, Isothermal oxidation behavior of ferritic oxide dispersion strengthened alloy at high temperatures, *J. Eng. Technol. Sci.*, 54 (2), 220210.

[5] Safarzadeh, O., and Qarani-tamai, M., 2021, Full-core reactor physics analysis for accident tolerant cladding in a VVER-1000 reactor, *Ann. Nucl. Energy*, 155, 108163.

[6] Khoshahval, F., 2024, Neutron-physical characteristics of UO_2 and UN/U_3Si_2 fuels with Zr, SiC and APMT accident tolerant claddings, *Radiat. Phys. Chem.*, 222, 111869.

[7] Menghani, J., Vyas, A., More, S., Paul, C., and Patnaik, A., 2021, Parametric investigation and optimization for CO_2 laser cladding of AlFeCoCrNiCu powder on AISI 316, *High Temp. Mater. Processes*, 40 (1), 265–80.

[8] Verma, L., and Dabhade, V.V., 2023, Synthesis of Fe-15Cr-2W oxide dispersion strengthened (ODS) steel powders by mechanical alloying, *Powder Technol.*, 425, 118554.

[9] Wang, X., Zhang, D., Darsell, J.T., Ross, K.A., Ma, X., Liu, J., Liu, T., Prabhakaran, R., Li, L., Anderson, I.E., and Setyawan, W., 2024, Manufacturing Oxide Dispersion Strengthened (ODS) steel plate via cold spray and friction stir processing, *J. Nucl. Mater.*, 596, 155076.

[10] Ren, J., Yu, L. Liu, C., Ma, Z., Li, H., Wang, Z., Liu, Y., and Wang, H., 2022, Creep properties, microstructural evolution, and fracture mechanism of an Al added high Cr ODS steel during creep deformation at 600 °C, *J. Nucl. Mater.*, 558, 153376.

[11] Singh, R., Prakash, U., Kumar, D., and Laha, K., 2023, Development of creep resistant high yttria 18Cr ferritic ODS steel through hot powder forging route, *J. Nucl. Mater.*, 584, 154566.

[12] Pawawoi, P., Prajitno, D.H., Dewi, A.A., and Manaf, A., 2019, High-temperature oxidation behavior of Fe-18Al alloy added with 2 %ZrO_2 nanoparticles, *IOP Conf. Ser.: Mater. Sci. Eng.*, 515, 012027.

[13] Ke, L., Meng, L., Fang, S., Lin, C., Tan, M., and Qi, T., 2023, High-temperature oxidation behaviors of $AlCrTiSi_{0.2}$ high-entropy alloy doped with rare earth La and Y, *Crystals*, 13 (8), 1169.

[14] Zheng, Z., Wang, S., Long, J., Wang, J., and Zheng, K., 2020, Effect of rare earth elements on high temperature oxidation behaviour of austenitic steel, *Corros. Sci.*, 164, 108359.

[15] Bai, B., Han, X., Cao, H., He, X., Zhang, C., and Yang, W., 2022, Composition optimization of radiation resistance ODS alloy with high strength and ductility for advanced reactor based on machine learning, *J. Nucl. Sci. Technol.*, 59 (6), 725–734.

[16] Xu, S., Zhou, Z., Zheng, W., and Jia, H., 2019, Mechanical properties evaluation and plastic instabilities of Fe-9%Cr ODS steels, *Fusion Eng. Des.*, 149, 111335.

[17] Zinkle, S.J., Boutard, J.L., Hoelzer, D.T., Kimura, A., Lindau, R., Odette, G.R., Rieth, M., Tan, L., and Tanigawa, H., 2017, Development of next generation tempered and ODS reduced activation ferritic/martensitic steels for fusion energy applications, *Nucl. Fusion*, 57 (9), 092005.

[18] Ren, J., Yu, L., Liu, Y., Liu, C., Li, H., and Wu, J., 2018, Effects of Zr addition on strengthening mechanisms of Al-alloyed high-Cr ODS steels, *Materials*, 11 (11), 118.

[19] Schappel, D., and Capps, N., 2024, Impact of LWR assembly structural features on cladding burst behavior under LOCA conditions, *Nucl. Eng. Des.*, 418, 112887.

[20] Gausse, C., Dunlop, C.W., Friskney, A.A., Stennett, M.C., Hyatt, N.C., and Corkhill, C.L., 2020, Synthesis, characterisation and preliminary corrosion behaviour assessment of simulant Fukushima nuclear accident fuel debris, *MRS Adv.*, 5 (1), 65–72.

[21] Gao, J., Song, P., Huang, Y.J., Yabuuchi, K., Kimura, A., Sakamoto, K., and Yamashita, S., 2019, Effects of neutron irradiation on 12Cr–6Al-ODS steel with electron-beam weld line, *J. Nucl. Mater.*, 524, 1–8.

[22] Seils, S., Kauffmann, A., Delis, W., Boll, T., and Heilmaier, M., 2021, Microstructure and mechanical properties of high-Mn-ODS steels, *Mater. Sci. Eng., A*, 825, 141859.

[23] Zhao, M., Zhang, P., Xu, J., Ye, W., Yin, S., Zhao, J., Qiao, Y., and Yan, Y., 2024, Optimization of microstructure and tensile properties for a 13Cr-1W ODS steel prepared by mechanical alloying and spark plasma sintering using pre-alloyed powder, *Mater. Charact.*, 207, 113581.

[24] Yang, T.X., Li, Z.X., Zhou, C.J., Xu, Y.C., and Dou, P., 2023, Effects of Zr and/or Ti addition on the morphology, crystal and metal/oxide interface structures of nanoparticles in FeCrAl-ODS steels, *J. Nucl. Mater.*, 585, 154613.

[25] Kaushik, G.N., Nagini, M., Reddy, M.S.P., Hebalkar, N.Y., Vijay, R., and Murty, B.S., 2022, Effect of Zr and ZrO_2 on aqueous corrosion behaviour of oxide dispersion strengthened 9Cr ferritic-martensitic steels, *Mater. Lett.*, 324, 132428.

[26] Mansur, L.K., Rowcliffe, A.F., Nanstad, R.K., Zinkle, S.J., Corwin, W.R., and Stoller, R.E., 2004, Materials needs for fusion, Generation IV fission reactors and spallation neutron sources – Similarities and differences, *J. Nucl. Mater.*, 329-333, 166–172.

[27] Ijiri, Y., Oono, N., Ukai, S., Ohtsuka, S., Kaito, T., and Matsukawa, Y., 2016, Oxide particle–dislocation interaction in 9Cr-ODS steel, *Nucl. Mater. Energy*, 9, 378–382.

[28] Basuki, E.A., Rahmaputra, F., Rabbani, N.A., Ardiansyah, S., Khan, A.M., Korda, A., Muhammad, F., and Prajitno, D.H., 2018, Effects of milling time on the microstructures of sintered Fe-16Cr-4Al-0.4Y_2O_3 ODS ferritic steel, *Nanotechnol. Perceptions*, 14 (2), 99–108.

[29] Rabbani, N.A., 2017, Studi Evolusi Mikrostruktur Baja Feritik ODS Hasil Perlakuan Milling dan Sintering dengan Metode Pembuatan Cold Compaction dan Solid-State Sintering, *Undergraduate Thesis*, Bandung Institute of Technology, Bandung, Indonesia.

[30] Basuki, E.A., 2016, *Panduan Logam untuk Aplikasi Temperatur Tinggi dan Penghematan Energi*, ITB Press, Indonesia.

[31] Tomaszewicz, P., and Wallwork, G.R., 1983, Observations of nodule growth during the oxidation of pure binary iron-aluminum alloys, *Oxid. Met.*, 19 (5), 165–185.

[32] Cornell, R.M., and Schewertmann, U., 2000, *The Iron Oxides: Structure, Properties, Reactions, Occurences and Uses*, Wiley-VCH, Weinheim, Germany.

[33] Grewal, H.S., Sanjiv, R.M., Arora, H.S., Kumar, R., Ayyagari, A., Mukherjee, S., and Singh, H., 2017, Activation energy and high temperature oxidation behavior of multi-principal element alloy, *Adv. Eng. Mater.*, 19 (11), 1700182.